


## Article

# Comprehensive Analysis of the Failure Potential of a Motorway Landslide in Dabu County, China

Sheng Chen <sup>1,2</sup>, Yang Hao <sup>3,\*</sup> , Wencai Zhang <sup>1,2</sup>, Ying Sun <sup>1,2</sup> and Xue Liu <sup>1,2</sup><sup>1</sup> CCCC Fourth Harbor Engineering Institute Co., Ltd., Guangzhou 510230, China<sup>2</sup> CCCC Key Laboratory of Environment Protection and Safety in Foundation Engineering of Transportation, Guangzhou 510230, China<sup>3</sup> State Key Laboratory of Intelligent Construction and Healthy Operation and Maintenance of Deep Underground Engineering, China University of Mining and Technology, Xuzhou 221116, China

\* Correspondence: yanghao@cumt.edu.cn; Tel.: +86-18-63-613-6908

**Abstract:** Because the failure potential of a landslide is difficult to assess, a motorway landslide that has obviously deformed was used as a case study in this research. Several multi-integrated geotechniques, including field investigation, drilling, electrical resistivity tomography (ERT), stability analysis, and numerical simulations, were used to achieve this goal. Field investigation with drilling was used to roughly determine the failure potential mass boundary and the material composition. ERT technique was further used to distinguish the structure and composition of underground materials; the results agreed well with the field investigation, as well as the drilling data in the lithology judgement. The above investigations also showed the failure potential mass is in a slow sliding state and the slip surface roughly follows the contact zone between the upper soil and bedrock. Next, stability analysis based on the limit equilibrium method (LEM) was used to judge the current stability status of the slope, and its factor of safety (FOS) was 1.2 under the natural condition, 1.05 under the earthquake condition, and 1.15 under the rainfall condition. Based on the assessed potential slip surface and digital elevation data, a three-dimensional smoothed particle hydrodynamics (SPH) model was used to simulate the failure potential process. The dynamic information of the run-out behavior, including velocity, movement distance, and frictional energy, can be obtained, which is useful for hazard prediction.



**Citation:** Chen, S.; Hao, Y.; Zhang, W.; Sun, Y.; Liu, X. Comprehensive Analysis of the Failure Potential of a Motorway Landslide in Dabu County, China. *Water* **2023**, *15*, 2675. <https://doi.org/10.3390/w15142675>

Academic Editor: Stefano Luigi Gariano

Received: 28 June 2023

Revised: 20 July 2023

Accepted: 20 July 2023

Published: 24 July 2023



**Copyright:** © 2023 by the authors. Licensee MDPI, Basel, Switzerland. This article is an open access article distributed under the terms and conditions of the Creative Commons Attribution (CC BY) license (<https://creativecommons.org/licenses/by/4.0/>).

**Keywords:** landslide; smoothed particle hydrodynamics; electrical resistivity tomography; dynamic analysis; failure potential forecasting

## 1. Introduction

Landslides are among the most catastrophic and frequent geological disasters in nature, causing great losses for human beings [1–4]. There is a large number of slopes that have high potential to slide and form landslides due to their material properties or external loads such as rainfall, earthquakes, or excavation [5,6]. Although some of these have traits such as crown cracks and a deformation crest to show they have high potential to fail in a short time [7,8], their failure potentials, including the potential sliding zone and potential landslide deposit area, are difficult to determine, and there is no mature method for studying them. This creates great challenges for landslide prediction and prevention. Considering there are many metastable slopes in mountainous engineering areas, such as the Three Gorges Reservoir Area [9,10], it is essential to judge the failure potential area of these metastable slopes to avoid potential landslides causing great losses.

In recent years, many geotechniques have been developed for landslide investigation and assessment. Traditional methods to study the failure potential area of the slope rely on field investigation and drilling technology, which can roughly determine the failure potential mass [5]. However, using these methods, it is difficult to quantitatively acquire the failure potential area or slip surface. With the development of geotechniques, some

semi-quantitative or quantitative methods can be used to quantitatively investigate landslides, and to further help determine the potential slip surface. For example, remote sensing helps to easily visualize the scene and topographic conditions. Multiperiod remote sensing and interferometric synthetic aperture radar (InSAR) help to determine the scale of the failure potential mass by judging a large deformation area [11,12]. Geophysical prospecting techniques, which use various geophysical fields to detect the variation in geological conditions, have become popular in engineering geology. The electrical resistivity tomography (ERT) technique has been used in landslide investigations, and it can reveal the geological structure and material composition [13–17]. The limit equilibrium method (LEM) can be used to determine the most dangerous slip surface and factor of safety by static analysis when lithology and mechanical parameters are known [5], providing an important way to assess the failure potential area. Based on knowing the failure potential area, numerical simulation can be used to assess the post-failure run-out process and affected area. Many numerical methods can be used for landslide simulation, such as the discrete element method (DEM) [18–21], smoothed particle hydrodynamics (SPH) [22,23], the material point method (MPM) [24,25], and the depth-integrated flow method (DIFM) [26,27]. In addition, geotechnical reliability analysis (GRA) also provides a novel way to evaluate slope stability from a probabilistic perspective, and has gained increasing attention in the past two decades [28–30]. The application of the above geotechniques has helped researchers to quantitatively assess the failure potential of a landslide.

In this paper, the authors proposed an integrated method to assess the failure potential of a motorway landslide that has deformed obviously but does not slide. A field investigation was first used to roughly assess the boundary of the metastable part of the slope, which can be considered as the failure potential mass. Then, the ERT technique with drilling was applied to further investigate the underground structure and composition. Later, the LEM was used to assess the current stability status, to determine whether failure potential assessment is needed. After determining the failure potential slip surface, a numerical simulation for failure potential assessment based on SPH was carried out, and the failure-potential-affected area was acquired. A flowchart of the above geotechniques and processes is shown in Figure 1. This manuscript provides an integrated geotechniques-based approach for potential landslide failure assessment, which can be used for disaster prevention and mitigation.

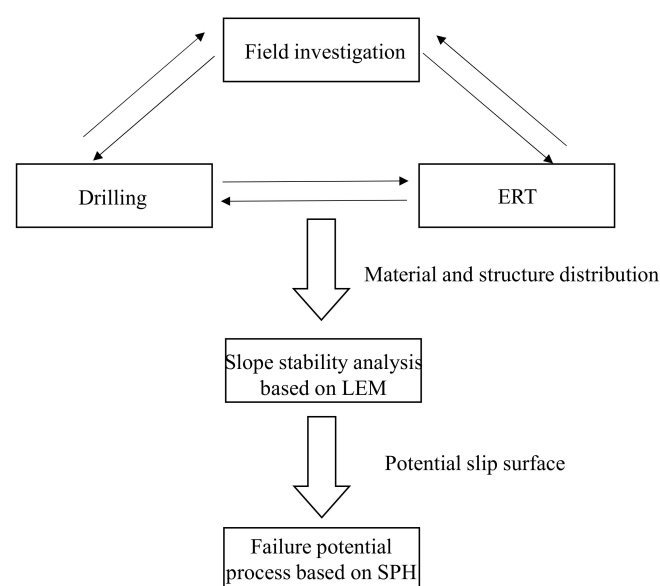


**Figure 1.** Flowchart of this work.

## 2. Background

### 2.1. Study Area

The Dabu landslide is located in Dabu county, northwest of Guangdong province (Figure 2a). The study area belongs to the low hilly landform (Figure 2b). Because it suffers from strong erosion, valleys are frequently narrow and deep in the study area. The mountainous slopes are generally between  $15^\circ$  and  $30^\circ$ .

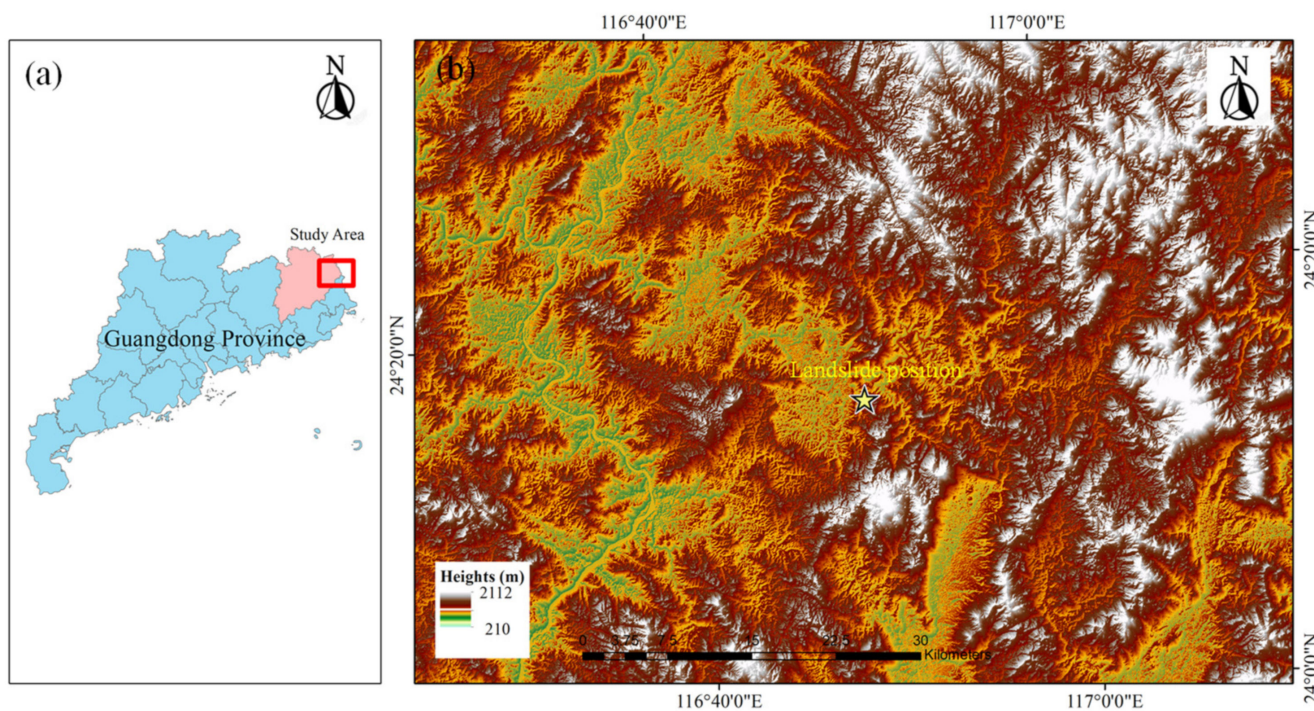


**Figure 2.** The study area: (a) general location of the landslide; (b) specific location and topographic condition of the landslide (the source data is based on SRTM with the resolution of 30 m).

The study area has undergone a transformation including multiple tectonic movements, and, therefore, faults and fractures develop well. These faults further generate many geological disasters and control the scale of these geological disasters. The rock joints and fissures around the landslide are extremely developed, with poor integrity, high weathering, chaotic lithology, and poor continuity. The strata around the landslide are mainly composed of Quaternary sediments, Triassic mudrock, siltstone, and Permian limestone.

The study area has a relatively distinct rainy climate. The average annual rainfall is between 1300 and 1800 mm, concentrated from April to September. Surface runoff frequently occurs at the gully, and seepage further promotes the occurrence of landslides.

### 2.2. Dabu Landslide

Dabu landslide is located on a high slope belonging to an old landslide deposit near a motorway (Figure 3). The slope belongs to a cutting slope and an anchor frame covers the middle part of the slope. The composition of the landslide is silty clay, gravel, and mudrock with gravel. The strongly weathered mudrock is the main body of the slope, with gravels and mudrock unevenly distributed inside the slope. The slope has not slid but has obviously deformed. Excavation is considered to be the direct triggering factor causing the landslide because it changes the original stable stress status and provides space for slope deformation. Concentrated rainfall is also considered an important triggering factor because it can infiltrate the fractured rock and be collected in the rock, increasing the gravity of soils and rocks. In addition, rainfall can soften mudrock as well as clay, reducing the strength of the materials. The potential sliding boundary of the metastable part can be

determined from the landform. The rear edge of the landslide is in the shape of a circular chair. The average width of the landslide is about 100 m, while the average length of the landslide is about 120 m. The area covered by the landslide is about 8300 m<sup>2</sup>. The average landslide thickness is 16 m and the total volume of the metastable part is  $13 \times 10^4$  m<sup>3</sup>. The relative height difference between the front and rear edges is 55 m.

During a field investigation in 2017, metastability phenomena of the slope such as cracks and a terrain bulge can be observed. It was observed that a drop head formed at the crest of the landslide (Figure 4a). The drop head can reach the maximum height of 3 m and maximum width of 3 m. In addition, a large horizontal crack formed at the trailing edge of the landslide with the length of 38 m and width between 0.2 and 0.4 m (Figure 4b). At the middle part of the slope, part of the anchor frame was cut by slope deformation and creep (Figure 4c). Due to different displacements of different parts, some vertical cracks formed. Obvious deformation also occurred at the front edge of the landslide. Soil around the landslide shear outlet obviously deformed with some soil blocks falling off (Figure 4d). After the rainy season in June 2018, the landslide deformation continued to increase. The maximum height of the drop head increased from 3 to 5 m, and the width increased to 5 m, indicating the metastable part of the slope continued deforming and has a great possibility to slide in the future. Once the slope has slid, the landslide would destroy the motorway, causing the losses of human lives and properties.

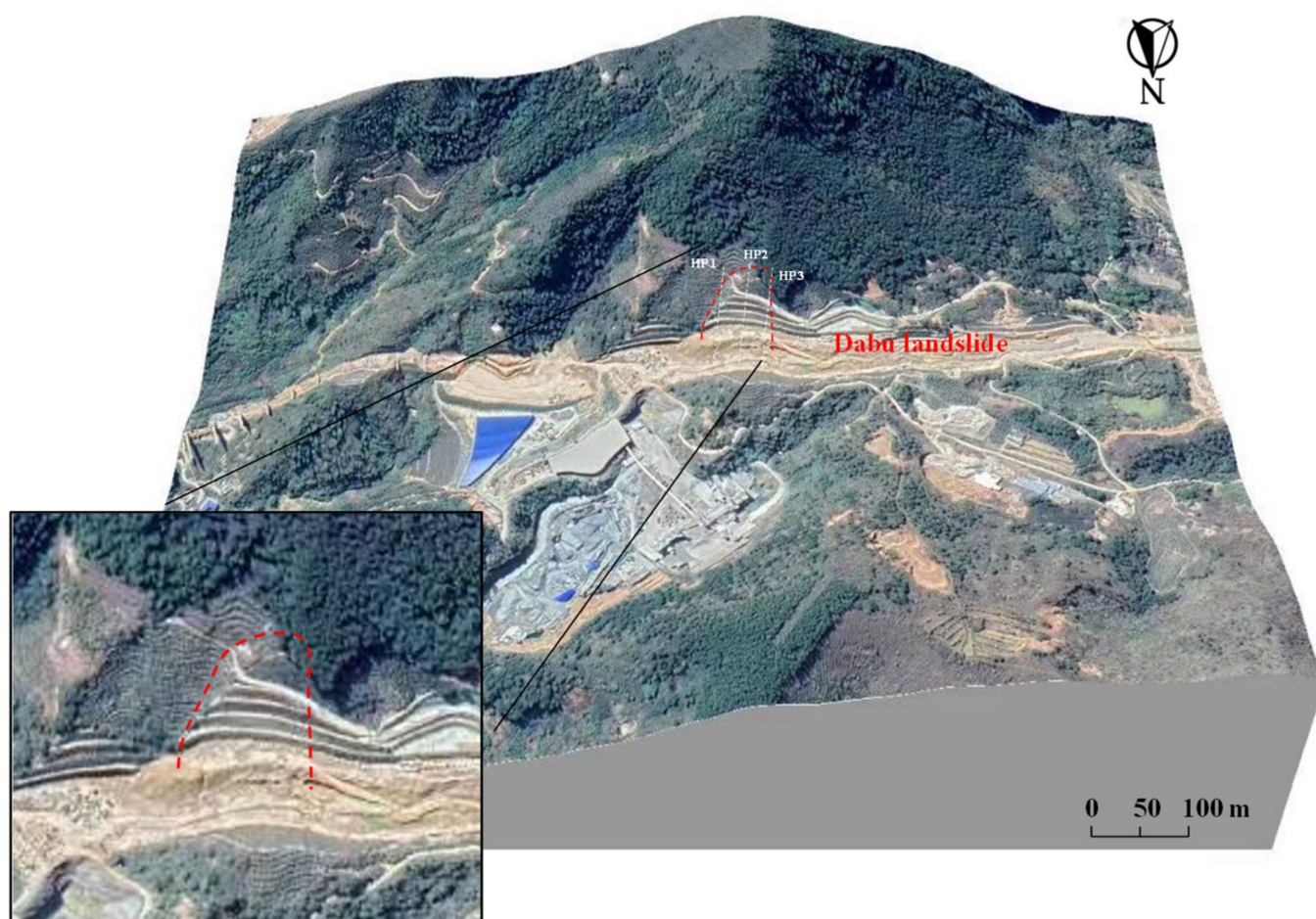


**Figure 3.** Overview of the Dabu landslide based on remote sensing (the photograph of the waste dump was taken on 12 March 2016).

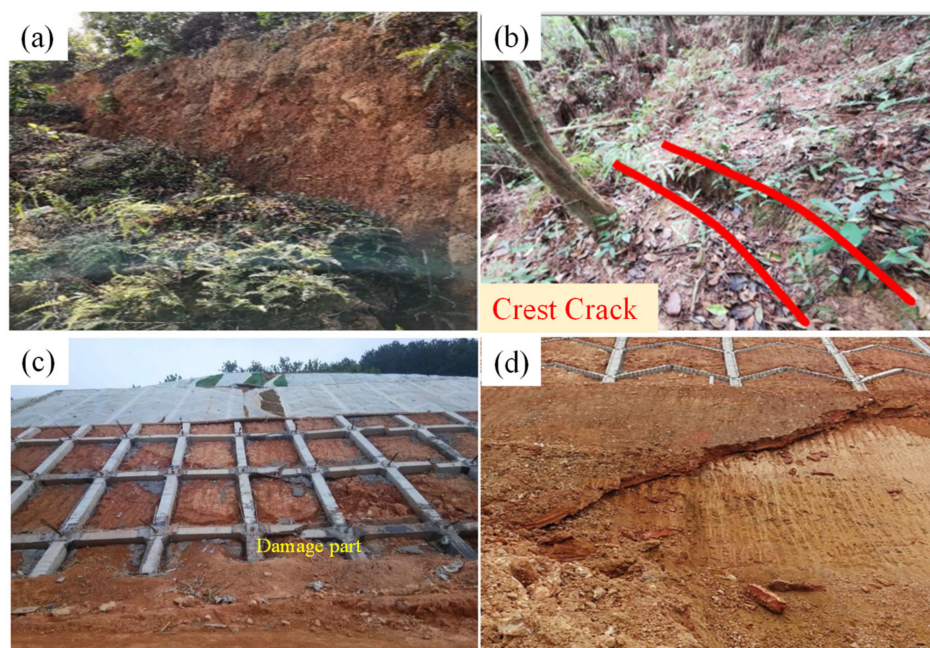


**Figure 4.** Deformation characteristics of Dabu landslide: (a) drop head; (b) crest crack; (c) damaged part of the anchor frame; (d) crest crack of the landslide.

### 3. Failure Potential of Dabu Landslide

#### 3.1. Electrical Resistivity Tomography Analysis

ERT is a non-invasive geophysical prospecting method for imaging lateral and vertical variation in subsurface resistivity, and for indirectly mapping geological features. It is an electro-exploration method that applies an electrical difference to different materials to distinguish geological bodies with different resistivities by utilizing the distribution of electricity within electric fields. Based on its characteristics, it was applied to help examine the underground composition and structure, which were difficult to observe directly. In this paper, the EDGMD-1 electric apparatus (DFDK Inc., Chongqing, China) was used. Three ERT profiles were set for the examination, named HP1, HP2, and HP3, as shown in Figure 3. In each profile, 120 electrodes were used with a maximum electrode distance of 10 m. After finishing measuring resistivity, the Surfer software was used to process and draw the contour map of resistivity. According to field experience, the low resistivity of the mudrock is from 10 to 100  $\Omega\text{m}$ ; the relatively low resistivity of the argillaceous siltstone is from 100 to 280  $\Omega\text{m}$ ; the medium resistivity of the Quaternary deluvial gravelly soil is from 280 to 500  $\Omega\text{m}$ ; and the high resistivity of the malmstone is above 500  $\Omega\text{m}$ , combined with the drilling data. If the rock and soil have a higher water content, the resistivity significantly decreases. In addition, in places where resistivity is distorted there often exists discontinuous structures such as faults. The underground composition and structure can be judged by resistivity.

Figure 5 shows the ERT results of the three profiles. From the profile of HP1, it can be found that the upper resistivity of the slope is obviously greater than the lower resistivity of the slope. In addition, the resistivity of the upper part of the slope obviously varies along the section. A similar phenomenon was observed from the HP2 and HP3 profiles. In the horizontal scale from 0 to 150 m, materials at the top of the slope are generally greater than 500  $\Omega\text{m}$ , indicating the materials are mainly composed of malmstone. In the upper part of the slope with the horizontal scale from 150 to 450 m, materials are unevenly distributed argillaceous siltstone, Quaternary deluvial gravelly soil, and malmstone, and material under this bottom layer is mainly mudrock. Contour lines that bend intensely in the vertical direction frequently indicate that there is a vertical fault. The rapid change in the resistivity in the vertical direction indicates that there is an obvious contact interface

between mudrock and upper materials. Because the permeability of the upper materials is significantly greater than that of the lower mudrock, the rainwater can easily converge on the interface during rainfall, softening the contact interface. In addition, rainfall saturates the upper materials and increases their gravity and sliding force. Therefore, it is concluded that the contact zone between the upper materials and lower mudrock is the potential slip surface according to ERT results (Figure 6).

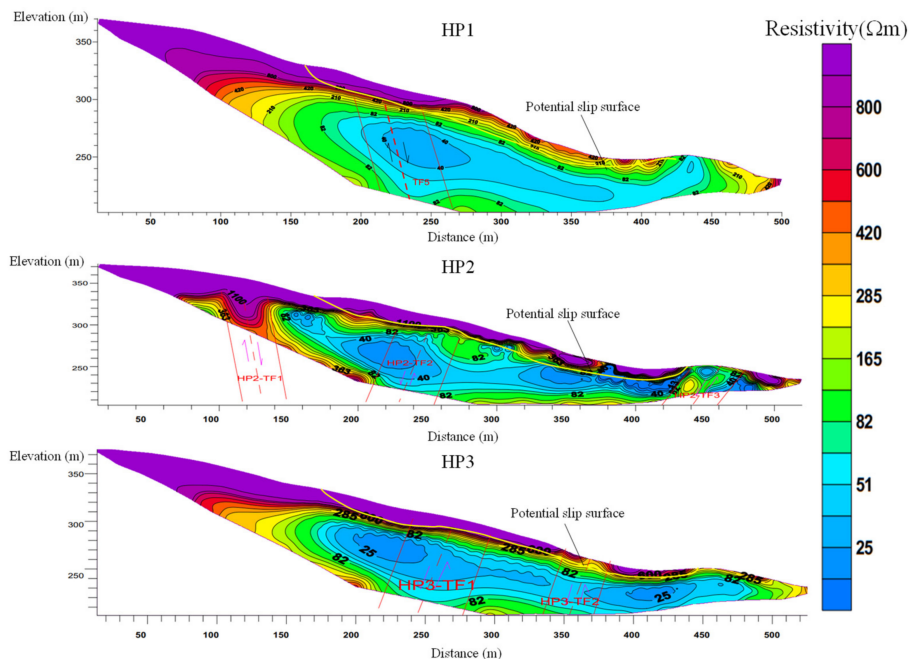


Figure 5. ERT inverse models for the investigated longitudinal profiles.

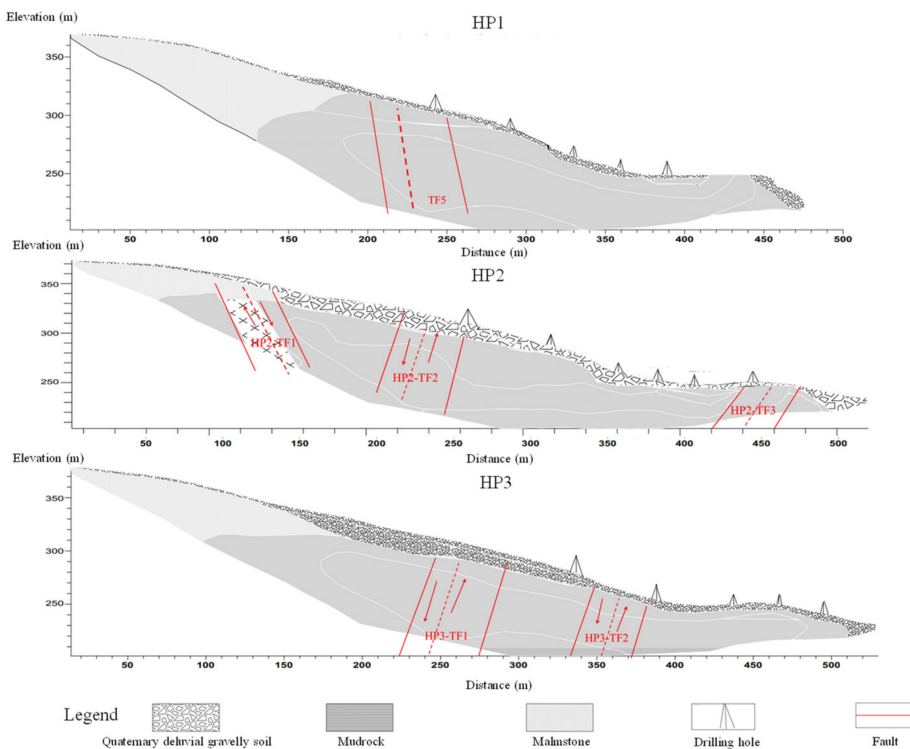
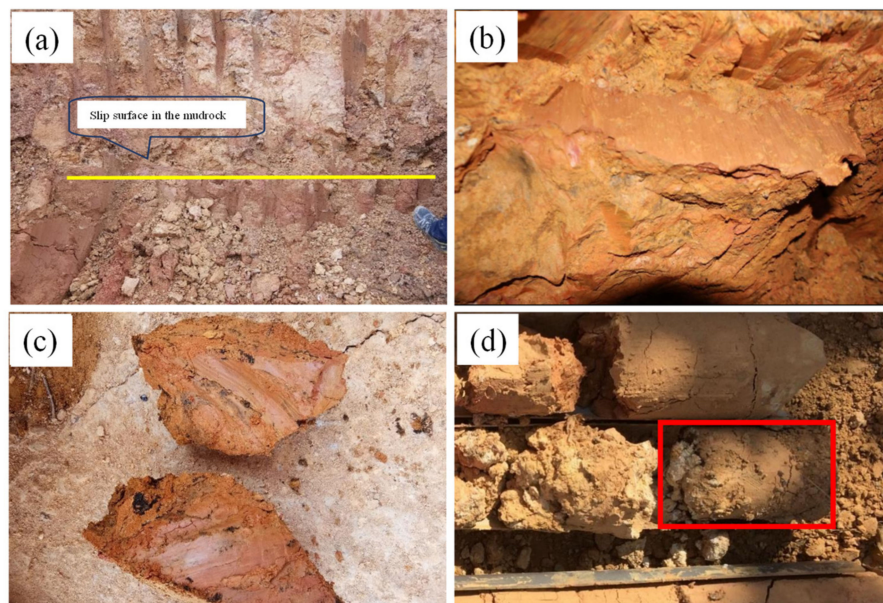


Figure 6. Concluded material composition from ERT results.

To further determine the potential slip surface, field investigation was used to validate ERT results. According to the field investigation, the main slip surface of the landslide is mainly the interior of the Quaternary silty clay with gravel at the middle and rear part (Figure 7a). The slip surface at the middle and front part is the contact zone between the gravel layer and mudrock, and the contact zone is generally the broken line. Stria can be observed from the concluded slip surface (Figure 7b).



**Figure 7.** Sliding phenomena of Dabu landslide from the investigation and drilling data: (a) slip surface in the mudrock and the yellow line denotes the position of the slip surface; (b) stria in the slip surface; (c,d) scratches on the soil samples in the red square.

A drilling technique was also used in the field investigation. Five holes were set in each profile of HP1, HP2, and HP3 to realize underground material composition and structure. The composition of materials at different depths is consistent with the ERT results. In addition, some samples collected from the holes present obvious scratches (Figure 7c,d), and it was concluded that these scratches were generated by relative movement of failure potential mass. Depths of these samples are mainly from 10 m to 30 m. Locations of these samples with scratches are highly consistent with the slip surface determined from ERT results, further indicating the contact surface is the potential slip surface. The thickness of the potential slip zone is from 0.5 to 3 m according to the drilling data.

### 3.2. Stability Analysis

The stability analysis of a slope is based on LEM. LEM is a classical and widely used method for the calculation of the FOS. LEM is used to statically analyze the slope stability. Because the slip surface is generated by shear damage, the FOS is defined as the ratio of the shear strength to the slide force on the slip surface in the LEM, as shown in Equation (1):

$$\text{FOS} = \frac{\int (c + \sigma \tan \varphi) dA}{\int \tau dA} \quad (1)$$

where  $c$  is the cohesion of material,  $\varphi$  is the internal angle of friction of material,  $\sigma$  is the normal compressive stress on slip surface, and  $\tau$  is the shear strength per unit area on the slip surface. The calculation of forces on the slip surface is based on discrete soil slices. In the LEM, many supposed slip surfaces of the slope are calculated to acquire the FOS, and the most critical slip surface corresponds to the minimum FOS value.

A large number of computational methods are used for LEM to calculate FOS, such as the Bishop method, Janbu method, Morgenstem–Price method, and unbalanced thrust transmission method. In each method, different assumptions and principles are adopted to fit different situations. In this paper, the unbalanced thrust transmission method is used for FOS calculation considering the slope has deformed obviously and generated unbalanced force. Based on the slice method, FOS in the unbalanced thrust transmission method can be expressed as follows:

$$FOS = \frac{\sum_{i=1}^{n-1} \left( (W_i((1 - r_u) \cos \alpha_i - A \sin \alpha_i) - R_{Di}) \tan \phi_i + C_i L_i \prod_{j=i}^{n-1} \psi_j \right) + R_n}{\sum_{i=1}^{n-1} \left[ (W_i(\sin \alpha_i + A \cos \alpha_i) + T_{Di}) \prod_{j=i}^{n-1} \psi_j \right] + T_n} \tag{2}$$

$$R_n = (W_n((1 - r_D) \cos \alpha_n - A \sin \alpha_n) - R_{Dn}) \tan \phi_n + C_n L_n \tag{3}$$

$$T_n = W_n(\sin \alpha_n + A \cos \alpha_n) + T_{Dn} \tag{4}$$

$$\prod_{j=i}^{n-1} \psi_j = \psi_i \psi_{i+1} \psi_{i+2} \cdots \psi_{n-1} \tag{5}$$

$$\psi_j = \cos(\alpha_i - \alpha_{i+1}) - \sin(\alpha_i - \alpha_{i+1}) \tan \phi_{i+1} \tag{6}$$

where  $W_i$  is the weight of the soil slice  $i$ ,  $C_i$  is the cohesive force of the soil slice  $i$ ,  $\phi_i$  is the friction angle of the soil slice,  $L_i$  is the length of the soil slice,  $\alpha_i$  is the dip angle of the soil slice,  $A$  is the earthquake acceleration,  $r_u$  is defined as the ratio of pore water pressure to upper load,  $R_{Di}$  is the resistance force of the soil slice  $i$ ,  $T_{Di}$  is the sliding force of the soil slice  $i$ ,  $R_n$  and  $T_n$  are total resistance force and sliding force.

After determining the potential slip surface, the FOS of the slope is calculated. The section of HP2 was selected as the computational section. The failure potential mass was sliced according to the shape of the potential slip surface. The slip surface in each slice approximates a straight line to ensure it has the same inclined angle. According to this principle, the potential slip surface was divided into 11 slides. Three kinds of situations in which the slope fails under natural gravity, rainfall, and an earthquake were set. For the rainfall condition, the slope was considered to be saturated and the shear strength of the soil was set as the saturated shear strength. Except for shear strength,  $r_u$  was set as 1 in the saturated slope part. For the earthquake condition, a horizontal acceleration load was applied to the slope. According to the Seismic Ground Motion Parameters Zonation Map of China GB18306-2015, the seismic horizontal acceleration was set as 0.1 g, and the seismic load was calculated using the pseudo-static method. Physical and mechanical parameters for calculation were obtained from laboratory tests, and are shown in Table 1.

**Table 1.** Mechanical properties of relevant materials.

Material Type	Natural State			Saturated State		
	Weight (kN/m <sup>3</sup> )	Cohesion C (kPa)	Friction $\phi$ (°)	Weight (kN/m <sup>3</sup> )	Cohesion C (kPa)	Friction $\phi$ (°)
Quaternary deluvial gravelly soil	20	5	32	21	4	30
Mud rock	19.5	14	15	20	13	14.1
Malmstone	22	14	28.5	22.5	13	27

Based on the Equations (2)–(6), the FOS was calculated. The results show that when the slope is under the natural condition, the FOS was 1.20. However, when the slope



experienced rainfall or an earthquake, the FOS value decreased sharply. The FOS of the slope was 1.15 under the rainfall condition, while the FOS was only 1.05 under the earthquake condition. The results show that the stability of the slope was sensitive to the level of the earthquake. According to the Technical Code for Building Slope Engineering (GB50330-2013) published by the Chinese Ministry of Housing and Urban-Rural Development, when the FOS of a slope is less than 1.35, the slope is considered unstable. Thus, forecasting the failure potential of the Dabu landslide is essential.

### 3.3. Landslide Potential Post-Failure Analysis

SPH is a continuum method and it uses pseudo-particles to represent landslides. The principle of the method is that each pseudo-particle in the computational domain is approximated by a variable field via an evolving interpolation scheme. The variable value of a particle of interest can be approximated by summing the contributions from a set of neighboring particles, which can be expressed as follows:

$$f(x) = \sum_j \frac{m_j}{\rho_j} f_j W(|x - x_j|, h) \tag{7}$$

where  $f(x)$  is a function of the particle position vector,  $\rho$  is the density of the particle,  $m$  is the mass of the particle, and  $W$  is the kernel function.

The particle movement follows Newton’s second law, which can be expressed in per unit volume:

$$\rho a = F \tag{8}$$

where  $a$  is the acceleration of the particle and  $F$  denotes the resultant force.

$$F = \rho g - \nabla p + \mu \nabla^2 u \tag{9}$$

The first term on the right side of the equal sign is gravity, the second term is the force generated by the pressure difference, and the third term is the shear force generated by the velocity difference.

The acceleration of a point  $i$  in space can be expressed as follows:

$$a_i = g - \frac{\nabla p_i}{\rho_i} + \frac{\mu \nabla^2 u_i}{\rho_i} \tag{10}$$

The movement of a node is calculated based on central difference method of Newton’s second law which is expressed as follows:

$$\dot{u}_{(i+1)}^N = \dot{u}_{(i)}^N + \Delta t_{(i+1)} \ddot{u}_{(i+\frac{1}{2})}^N \tag{11}$$

where  $\ddot{u}$  is the node acceleration,  $\dot{u}$  is the node speed,  $u^N$  is the degree of freedom (component of displacement or rotation), and the subscript  $(i)$  refers to the increment number in the explicit dynamics step

The rheological behavior of a landslide can be considered as a type of fluid that requires proper rheological equations in the SPH model. The hydrodynamic behavior of a landslide has frequently been treated as a Bingham fluid in the literature. A Bingham fluid is a type of non-Newtonian fluid that begins to flow when the yield stress of the material is greater than a certain value, and its fluidity is linear. The Bingham shear characteristics can be treated as follows (Bao et al. 2022):

$$\eta = \begin{cases} \eta_0 & \text{if } \tau < \tau_0 \\ \frac{1}{\dot{\gamma}} \left( \tau_0 + k \left( \dot{\gamma} - \frac{\tau_0}{\eta_0} \right) \right) & \text{if } \tau \geq \tau_0 \end{cases} \tag{12}$$

where  $\eta$  is the viscosity,  $\tau$  is the shear stress,  $\dot{\gamma}$  is the shear strain rate,  $\eta_0$  is the shear viscosity at low shear rates,  $\tau_0$  is the yield shear stress at low shear rates,  $k$  is the flow

consistency index, and  $n$  represents the flow behavior indices. In the model, the parameters  $\eta_0$ ,  $\tau_0$ , and  $k$  need to be defined.

As a fluid, the equation of state (EOS) can be used to describe the behavior of the debris flow, which is expressed as follows:

$$p = \frac{\rho_0 c_0^2 \eta}{(1 - s\eta)^2} \left( 1 - \frac{\Gamma_0 \eta}{2} \right) + \Gamma_0 \rho_0 E_m \quad (13)$$

where  $\rho$  is the material's density,  $\sigma$  is the Cauchy stress,  $b$  is the body force,  $\rho_0$  is the reference density,  $c_0$  is the reference sound speed,  $s$  and  $\Gamma_0$  are material constants, considered 0 in fluid simulation [1], and  $E_m$  is the internal energy per unit mass.

To know the failure potential area of the Dabu landslide, the SPH method was used to simulate its post-failure dynamic process. To construct a 3D SPH landslide model, the digital terrain model (DTM) data with an accuracy of 5 m was used. The DTM data determine the current ground surface shape. As for the failure potential sliding mass, it was determined by failure potential slip surfaces in Figure 5, and then it was extracted via the 3D CAD software Rhino. The terrain of the slip surface, as well as the run-out path, were set as rigid shell elements while the sliding mass was set as SPH elements composed of 36,840 particles. The rheological parameters can be adopted empirically from Pellegrino's study [31]. In Pellegrino's study, yield shear stress  $\tau_0$  mainly ranges from several Pa to hundreds of Pa,  $\eta_0$  mainly ranges from a few tenths to several Pa.s,  $k$  mainly ranges from 0 to several tens, and  $\tau_0$  and  $\eta_0$  increase with increasing solid volumetric concentration. Considering the solid volumetric concentration of the potential landslide can be different, a group of lower values of  $\tau_0 = 0.2$  Pa,  $\eta_0 = 0.4$  Pa s, corresponding to solid volumetric concentration equaling 15% with high rheological mobility, a group of medium values of  $\tau_0 = 1.2$  Pa,  $\eta_0 = 1$  Pa s, corresponding to solid volumetric concentration equaling 30% with medium rheological mobility, and a group of higher values of  $\tau_0 = 100$  Pa,  $\eta_0 = 10$  Pa s, corresponding to solid volumetric concentration equaling 45% with low rheological mobility, were set for sensitivity analysis. As for the friction coefficient between the failure potential mass and the slip surface, a residual friction with a value of 0.36 ( $20^\circ$ ), which was obtained from the laboratory test, was adopted. The density of the sliding mass was set as  $2000 \text{ kg/m}^3$  according to the laboratory test. Considering the main movement of the giant landslides usually lasts for tens of seconds [5,7], the simulation time was set as 150 s, which was enough for post-failure simulation. Figure 8 shows the initial state of the numerical model.

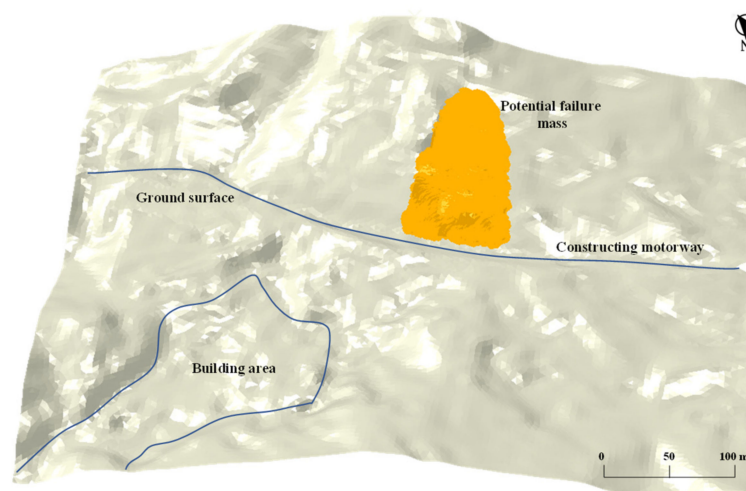


**Figure 8.** Three-dimension SPH model of the Dabu landslide.

Figure 9 shows the final failure potential area of the landslide under different rheological conditions. The simulation result shows that with the increase in sliding mass rheology, the failure potential area increases slightly, but the failure potential area differences under different rheological conditions are small in general. An important reason to ensure that the failure potential difference is not obvious is that terrain bulge limits the longitudinal movement of the landslide. The sliding mass mainly moves laterally and the maximum movement distance of the whole sliding mass is about 200 m. If the landslide occurred, the maximum deposit length along the motorway can reach 400 m under the high mobility condition, thus threatening engineering construction and human lives.

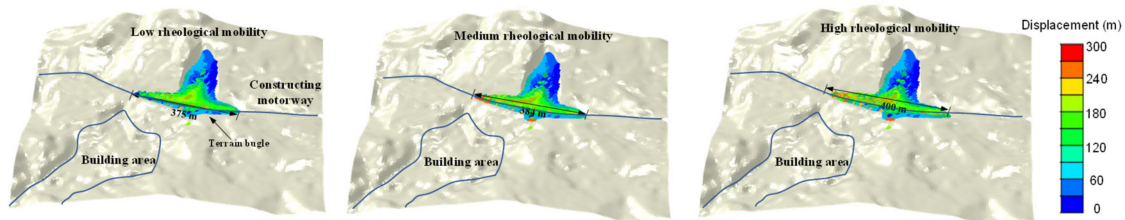


Figure 9. Final failure potential area of the landslide under different rheological conditions.

To further quantitatively determine how the rheological characteristics of the sliding mass affect landslide mobility, the authors summarized the landslide kinetic energy, frictional energy, and viscous energy under different rheological conditions (Figure 10). It can be found that kinetic energy increases with rheological mobility. The frictional energy also increases with rheological mobility. The reason for this phenomenon is that a sliding mass with high rheological mobility has a greater movement distance, generating greater frictional energy. As for the viscous energy, it decreases with rheological mobility. This is because a sliding mass with higher rheological mobility has lower viscosity, so its viscous energy should be smaller. The same law with the movement distance is that energies are not very different under different conditions because of limited movement distance.

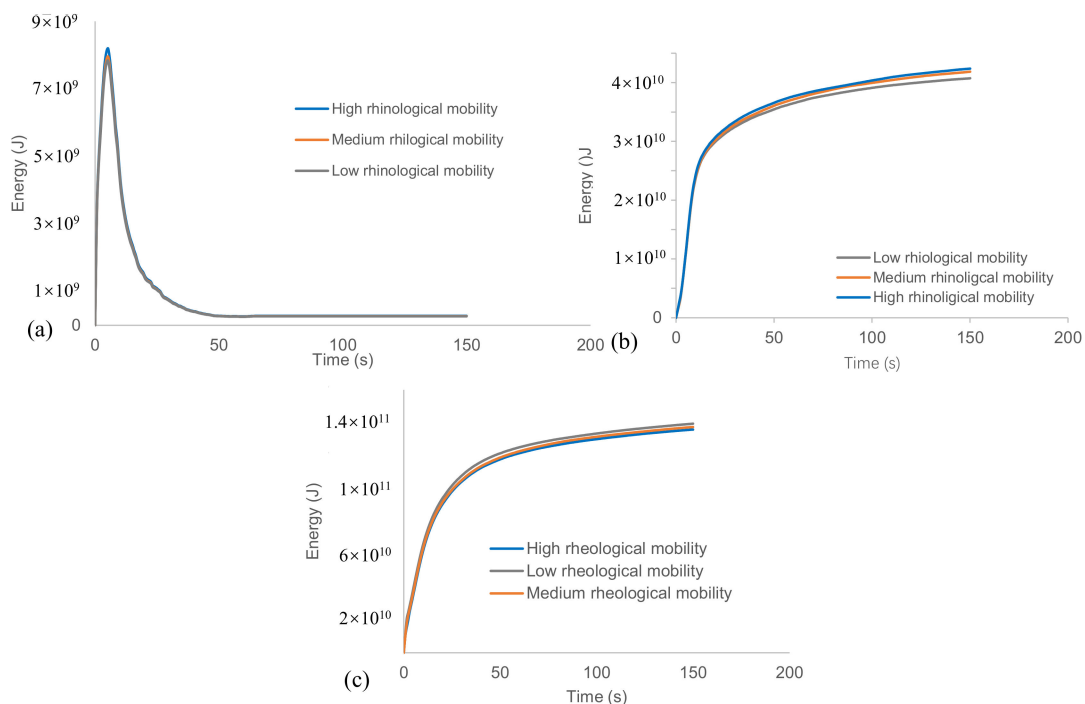
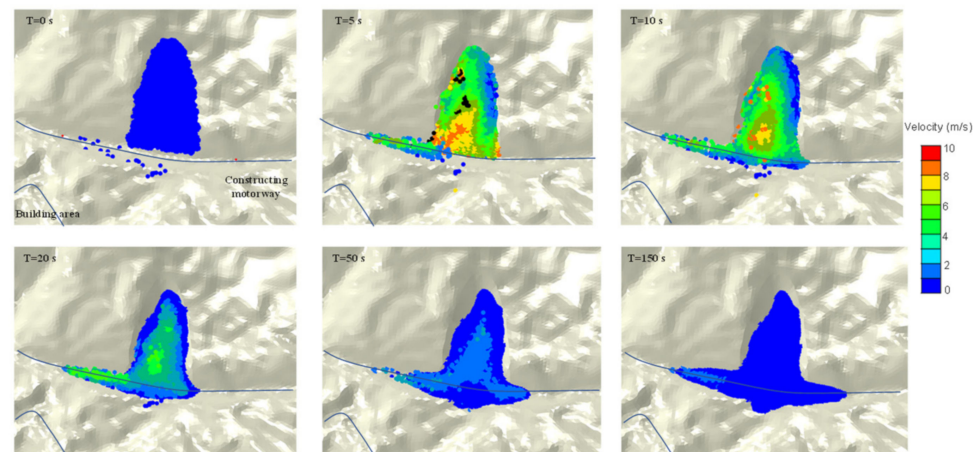
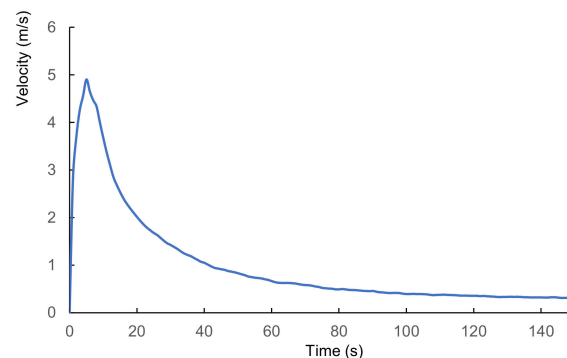


Figure 10. Variation in the kinetic energy, frictional energy, and viscous energy under different rheological conditions ((a–c) represent kinetic energy, frictional energy, and viscous energy, respectively).

Understanding the dynamic landslide process is important. To realize the dynamic process of the failure potential landslide, the medium rheological mobility condition was chosen for the analysis. Figure 11 shows the dynamic process of the Dabu landslide at different times of 0 s, 5 s, 10 s, 20 s, 50 s, and 150 s. To further quantitatively realize landslide mobility, the average movement speed of the whole sliding mass was also recorded, as shown in Figure 12. It shows that the potential sliding mass generally has two periods of acceleration and deceleration. In the acceleration period, the sliding mass rapidly accelerates during the initial few seconds after slope failure. At the time of 5 s, the sliding mass reaches the maximum speed of 5 m/s. The sliding mass reaches the bottom of the slope, and the front sliding mass rapidly decelerates due to collision with the terrain. The front sliding mass moves laterally due to the terrain bugle, and the back sliding mass also decelerates. Therefore, the sliding mass starts showing deceleration in general after 5 s. The sliding mass constantly decelerates, and the deceleration rate also constantly decreases with time. After 50 s, the movement speed of the sliding mass decreases below 1 m/s, and then the sliding mass slowly spreads until it completely stops.



**Figure 11.** Dynamic process of the Dabu landslide at different times.



**Figure 12.** Average movement speed of the sliding mass.

#### 4. Discussion

There is no direct way to judge the failure potential of a metastable slope at present and this paper proposed a method based on multi-integrated geotechniques to achieve this. In general, the integrated method is useful and can be used to successfully assess the potential post-failure scale of the landslide. The use of multi-integrated geotechniques to assess the failure potential of the landslide can not only provide useful information at each stage to ensure they are coherent, but also can be mutually verified to some extent. For example, the ETR analysis with drilling hole data, as well as LEM analysis, can be combined to more accurately judge the failure potential sliding mass. Although the methods based

on integrated geotechniques in this paper are useful, there are still some limitations. For example, two methods based on LEM and SPH were used for judging potential failure mass and post-failure movement analysis, respectively, but SPH has the potential to judge potential failure mass. Combining the judgement of potential failure sliding mass and post-failure movement analysis in one method is better than using two different methods to achieve the goal because it is difficult to transition perfectly during the using two methods. Developing a SPH model combining slope stability analysis, potential failure mass judgement, as well as post-failure dynamic analysis is important and meaningful. In addition, the SPH model used in this manuscript is a single-phase model but the sliding mass actually contains soil and water. A single-phase model cannot reflect the complex mechanism and process of water moving in soil. Using a fluid–solid coupling model is essential to further study the two phases of landslide movement [32–34].

Some geotechniques can be replaced with some other methods to fit different conditions. For example, post-failure dynamic analysis based on the SPH model can be replaced with a DEM model when the material is rock [35]. This is because DEM can reflect material fragmentation and separation, which are very important behaviors for a rockslide, while SPH model based on the continuum method cannot reflect these behaviors. If the dynamic deformation process is required in the slope stability analysis, LEM is not appropriate because it is based on the static analysis method and cannot reflect the deformation process. The finite element method (FEM) based on the strength reduction technique can calculate the FOS and reflect the deformation process at the same time [36]. In addition, FEM has the ability to analyze the dynamic seepage process under rainfall and the dynamic deformation process during an earthquake at the expense of more parameters. Using appropriate methods in the multi-integrated geotechniques is important.

## 5. Conclusions

In this paper, a comprehensive analysis was carried out to assess the failure potential of the Dabu landslide. Field investigation shows the slope is deforming slowly and has a high possibility of failing. ERT results combined with the drilling hole data show the boundary of the potential failure mass, whose average depth is from 10 to 20 m. Then, the slope stability was calculated via LEM, to acquire the current stability status under different conditions, including the natural state, rainfall condition, and earthquake condition. The outcomes show that the FOS of the slope is 1.2 under the natural condition, 1.05 under the earthquake condition, and 1.15 under the rainfall condition, so the slope was found to be metastable and may fail under the above conditions.

Then, a three-dimension SPH model was used to simulate a potential landslide under different solid volumetric concentration conditions. The results show that the water content of the sliding mass does not affect the potential movement speed and the deposit area is significantly restricted by the topography. If a potential landslide occurred, the landslide would affect motorway construction, and the maximum affected path could reach 400 m along the motorway. The main run-out process of the potential landslide can be divided into acceleration and deceleration periods. The acceleration period lasts for 5 s from slope failure to the point when the front sliding mass collides with terrain. It is worth noting that the final deposit area of the landslide might not vary much due to the limitation of the terrain even though the rheological properties of the materials vary greatly. This paper provides a useful integrated approach for landslide failure potential assessment, which can be used for disaster prevention and mitigation.

**Author Contributions:** Writing—original draft preparation, S.C.; project administration, Y.H.; funding acquisition, Y.H.; investigation, Y.H.; resources, W.Z., X.L. and Y.S.; data curation. All authors have read and agreed to the published version of the manuscript.

**Funding:** This research was funded by the National Natural Science Foundation of China (No. 52204114) and the Fundamental Research Program of Jiangsu Province (Natural Science Foundation)—Youth Fund Project (BK20210522).

**Data Availability Statement:** Not applicable.

**Acknowledgments:** We very thank for all the editors and reviewers who have helped us improve and publish the paper. Special thanks for Yiding Bao for helping us revise the manuscript.

**Conflicts of Interest:** The authors declare no conflict of interest.

## References

- Bao, Y.; Su, L.; Chen, J.; Ouyang, C.; Yang, T.; Lei, Z.; Li, Z. Dynamic process of a high-level landslide blocking river event in a deep valley area based on FDEM-SPH coupling approach. *Eng. Geol.* **2023**, *319*, 107108. [[CrossRef](#)]
- Ibañez, J.P.; Hatzor, Y.H. Rapid sliding and friction degradation: Lessons from the catastrophic Vajont landslide. *Eng. Geol.* **2018**, *244*, 96–106. [[CrossRef](#)]
- Tsuguti, H.; Seino, N.; Kawase, H.; Imada, Y.; Nakaegawa, T.; Takayabu, I. Meteorological overview and mesoscale characteristics of the Heavy Rain Event of July 2018 in Japan. *Landslides* **2019**, *16*, 363–371. [[CrossRef](#)]
- Song, D.; Shi, W.; Wang, C.; Dong, L.; He, X.; Wu, E.; Zhao, J.; Lu, R. Numerical Investigation of a Local Precise Reinforcement Method for Dynamic Stability of Rock Slope under Earthquakes Using Continuum–Discontinuum Element Method. *Sustainability* **2023**, *15*, 2490. [[CrossRef](#)]
- Bao, Y.; Chen, J.; Su, L.; Zhang, W.; Zhan, J. A novel numerical approach for rock slide blocking river based on the CEFDEM model: A case study from the Samaoding paleolandslide blocking river event. *Eng. Geol.* **2023**, *312*, 106949. [[CrossRef](#)]
- Zhao, B.; Wang, Y.-S.; Li, J.; Wang, J.-L.; Tang, C.-X. Insights into a giant landslide-prone area on the eastern margin of the Tibetan Plateau, China. *J. Mt. Sci.* **2021**, *18*, 21–37. [[CrossRef](#)]
- Bao, Y.; Li, Y.; Zhang, Y.; Yan, J.; Zhou, X.; Zhang, X. Investigation of the role of crown crack in cohesive soil slope and its effect on slope stability based on the extended finite element method. *Nat. Hazards* **2022**, *110*, 295–314. [[CrossRef](#)]
- Tang, L.; Zhao, Z.; Luo, Z.; Sun, Y. What is the role of tensile cracks in cohesive slopes? *J. Rock Mech. Geotech. Eng.* **2019**, *11*, 314–324. [[CrossRef](#)]
- Cao, S.; Xiang, W.; Wang, J.; Cui, D.; Liu, Q. Identifying the Groundwater Sources of Huangtupo Landslide in the Three Gorges Reservoir Area of China. *Water* **2023**, *15*, 1741. [[CrossRef](#)]
- Wang, R.; Zhao, K.; Wei, C.; Li, X.; Li, M.; Zhang, J. Study on the Soil Deterioration Mechanism in the Subsidence Zone of the Wildcat Landslide in the Three Gorges Reservoir Area. *Water* **2023**, *15*, 886. [[CrossRef](#)]
- Wang, Y.; Liu, D.; Dong, J.; Zhang, L.; Guo, J.; Liao, M.; Gong, J. On the applicability of satellite SAR interferometry to landslide hazards detection in hilly areas: A case study of Shuicheng, Guizhou in Southwest China. *Landslides* **2021**, *18*, 2609–2619. [[CrossRef](#)]
- Xu, Q.; Zheng, G.; Li, W.; He, C.; Dong, X.; Guo, X.; Feng, W. Study on successive landslide damming events of Jinsha River in Baige Village on October 11 and November 3. *J. Eng. Geol.* **2018**, *26*, 1534–1551.
- Peng, W.; Song, S.; Yu, C.; Bao, Y.; Sui, J.; Hu, Y. Forecasting Landslides via Three-Dimensional Discrete Element Modeling: Helong Landslide Case Study. *Appl. Sci.* **2019**, *9*, 5242. [[CrossRef](#)]
- Zhan, J.; Wang, Q.; Zhang, W.; Shangguan, Y.; Song, S.; Chen, J. Soil-engineering properties and failure mechanisms of shallow landslides in soft-rock materials. *Catena* **2019**, *181*, 104093. [[CrossRef](#)]
- Imani, P.; Tian, G.; Hadiloo, S.; Abd El-Raouf, A. Application of combined electrical resistivity tomography (ERT) and seismic refraction tomography (SRT) methods to investigate Xiaoshan District landslide site: Hangzhou, China. *J. Appl. Geophys.* **2021**, *184*, 104236. [[CrossRef](#)]
- Imani, P.; Tian, G.; EL-Raouf, A.A. Assessment of spatiotemporal changes in water contents of landslide zone by geophysical methods: A case study. *Arab. J. Geosci.* **2021**, *14*, 1380. [[CrossRef](#)]
- El-Raouf, A.A.; Iqbal, I.; Meister, J.; Abdelrahman, K.; Alzahrani, H.; Badran, O.M. Earthflow reactivation assessment by multichannel analysis of surface waves and electrical resistivity tomography: A case study. *Open Geosci.* **2021**, *13*, 1328–1344. [[CrossRef](#)]
- Bao, Y.; Zhai, S.; Chen, J.; Xu, P.; Sun, X.; Zhan, J.; Zhang, W.; Zhou, X. The evolution of the Samaoding paleolandslide river blocking event at the upstream reaches of the Jinsha River, Tibetan Plateau. *Geomorphology* **2020**, *351*, 106970. [[CrossRef](#)]
- Li, Y.; Chen, J.; Yan, J.; Zhou, F.; Wang, Q.; Li, Z.; Zhang, Y. Formation and evolution of a giant old deposit in the First Bend of the Yangtze River on the southeastern margin of the Qinghai-Tibet Plateau. *Catena* **2022**, *213*, 106138. [[CrossRef](#)]
- Li, Y.; Chen, J.; Zhou, F.; Bao, Y.; Li, Z.; Song, S.; Cao, C. Stability evaluation of rock slope based on discrete fracture network and discrete element model: A case study for the right bank of Yigong Zangbu Bridge. *Acta Geotech.* **2022**, *17*, 1423–1441. [[CrossRef](#)]
- Lo, C.-M.; Lin, M.-L.; Tang, C.-L.; Hu, J.-C. A kinematic model of the Hsiaolin landslide calibrated to the morphology of the landslide deposit. *Eng. Geol.* **2011**, *123*, 22–39. [[CrossRef](#)]
- Dai, Z.; Huang, Y. A three-dimensional model for flow slides in municipal solid waste landfills using smoothed particle hydrodynamics. *Environ. Earth Sci.* **2016**, *75*, 132. [[CrossRef](#)]
- Pastor, M.; Blanc, T.; Haddad, B.; Petrone, S.; Sanchez Morles, M.; Dremptic, V.; Issler, D.; Crosta, G.B.; Cascini, L.; Sorbino, G.; et al. Application of a SPH depth-integrated model to landslide run-out analysis. *Landslides* **2014**, *11*, 793–812. [[CrossRef](#)]
- Li, X.; Yan, Q.; Zhao, S.; Luo, Y.; Wu, Y.; Wang, D. Investigation of influence of baffles on landslide debris mobility by 3D material point method. *Landslides* **2020**, *17*, 1129–1143. [[CrossRef](#)]

25. Llano-Serna, M.A.; Farias, M.M.; Pedroso, D.M. An assessment of the material point method for modelling large scale run-out processes in landslides. *Landslides* **2016**, *13*, 1057–1066. [[CrossRef](#)]
26. Han, X.; Chen, J.; Xu, P.; Zhan, J. A well-balanced numerical scheme for debris flow run-out prediction in Xiaojia Gully considering different hydrological designs. *Landslides* **2017**, *14*, 2105–2114. [[CrossRef](#)]
27. Bao, Y.; Sun, X.; Chen, J.; Zhang, W.; Han, X.; Zhan, J. Stability assessment and dynamic analysis of a large iron mine waste dump in Panzhihua, Sichuan, China. *Environ. Earth Sci.* **2019**, *78*, 48. [[CrossRef](#)]
28. Wang, L.; Wu, C.; Gu, X.; Liu, H.; Mei, G.; Zhang, W. Probabilistic stability analysis of earth dam slope under transient seepage using multivariate adaptive regression splines. *Bull. Eng. Geol. Environ.* **2020**, *79*, 2763–2775. [[CrossRef](#)]
29. Zhang, W.; Wu, C.; Tang, L.; Gu, X.; Wang, L. Efficient time-variant reliability analysis of Bazimen landslide in the Three Gorges Reservoir Area using XGBoost and LightGBM algorithms. *Gondwana Res.* **2022**. [[CrossRef](#)]
30. Zhang, W.; Gu, X.; Hong, L.; Han, L.; Wang, L. Comprehensive review of machine learning in geotechnical reliability analysis: Algorithms, applications and further challenges. *Appl. Soft Comput.* **2023**, *136*, 110066. [[CrossRef](#)]
31. Pellegrino, A.M.; Anna, S.D.S.; Schippa, L. An integrated procedure to evaluate rheological parameters to model debris flows. *Eng. Geol.* **2015**, *196*, 88–98. [[CrossRef](#)]
32. Zhang, X.; Shu, C.; Fujii, M.; Wu, Y.; Sun, D.; Ye, P.; Bao, Y. Numerical and Experimental Study on Water-Heat-Salt Transport Patterns in Shallow Bare Soil with Varying Salt Contents under Evaporative Conditions: A Comparative Investigation. *J. Hydrol.* **2023**, *621*, 129564. [[CrossRef](#)]
33. Zhang, X.D.; Shu, C.J.; Wu, Y.J.; Ye, P.; Du, D.W. Advances of coupled water-heat-salt theory and test techniques for soils in cold and arid regions: A review. *Geoderma* **2023**, *432*, 116378. [[CrossRef](#)]
34. Zhang, X.D.; Wu, Y.; Zhai, E.; Ye, P. Coupling analysis of the heat-water dynamics and frozen depth in a seasonally frozen zone. *J. Hydrol.* **2021**, *593*, 125603. [[CrossRef](#)]
35. Shi, W.; Zhang, J.; Song, D.; Guo, Z.; Tang, G.; Han, D. The September 16, 2013, Numerical investigation of the seismic dynamic response characteristics of high-steep layered granite slopes via time–frequency analysis. *Environ. Earth Sci.* **2023**, *82*, 153. [[CrossRef](#)]
36. Bao, Y.; Han, X.; Chen, J.; Zhang, W.; Zhan, J.; Sun, X.; Chen, M. Numerical assessment of failure potential of a large mine waste dump in Panzhihua City, China. *Eng. Geol.* **2019**, *253*, 171–183. [[CrossRef](#)]

**Disclaimer/Publisher’s Note:** The statements, opinions and data contained in all publications are solely those of the individual author(s) and contributor(s) and not of MDPI and/or the editor(s). MDPI and/or the editor(s) disclaim responsibility for any injury to people or property resulting from any ideas, methods, instructions or products referred to in the content.